Anthropogenic Asian aerosols provide Fe to the North Pacific Ocean

Paulina Pinedo-González[a,b,1], Nicholas J. Hawco[a,c], Randelle M. Bundy[d], E. Virginia Armbrust[d], Michael J. Follows[e], B. B. Cael[f], Angelicque E. White[c], Sara Ferrón[c], David M. Karl[c], and Seth G. John[a]

[a]Department of Earth Sciences, University of Southern California, Los Angeles, CA 90089; [b]Lamont-Doherty Earth Observatory, Columbia University, Palisades, NY 10964; [c]Department of Oceanography, Daniel K. Inouye Center for Microbial Oceanography: Research and Education, University of Hawaii at Manoa, Honolulu, HI 96822 [d]School of Oceanography, University of Washington, Seattle, WA 98195; [e]Earth, Atmospheric, and Planetary Sciences, Massachusetts Institute of Technology, Cambridge, MA 02139; and [f]National Oceanography Centre, Southampton SO14 3ZH, United Kingdom

Edited by Edward A. Boyle, Massachusetts Institute of Technology, Cambridge, MA, and approved September 16, 2020 (received for review May 21, 2020)

Fossil-fuel emissions may impact phytoplankton primary productivity and carbon cycling by supplying bioavailable Fe to remote areas of the ocean via atmospheric aerosols. However, this pathway has not been confirmed by field observations of anthropogenic Fe in seawater. Here we present high-resolution trace-metal concentrations across the North Pacific Ocean (158°W from 25°to 42°N). A dissolved Fe maximum was observed around 35°N, coincident with high dissolved Pb and Pb isotope ratios matching Asian industrial sources and confirming recent aerosol deposition. Iron-stable isotopes reveal in situ evidence of anthropogenic Fe in seawater, with low δ^{56}Fe (−0.23‰ > δ^{56}Fe > −0.65‰) observed in the region that is most influenced by aerosol deposition. An isotope mass balance suggests that anthropogenic Fe contributes 21–59% of dissolved Fe measured between 35° and 40°N. Thus, anthropogenic aerosol Fe is likely to be an important Fe source to the North Pacific Ocean.

soluble iron | iron isotopes | lead isotopes | anthropogenic aerosols | coal burning

Iron (Fe) is a globally important micronutrient which is known to limit phytoplankton productivity in up to a third of the world's oceans (1). The deposition of aerosol Fe is an important source of Fe to surface waters of the open oceans, especially in the northern hemisphere. Aerosol Fe is conventionally thought to be dominated by lithogenic (mineral dust) material from arid regions (2). Yet, some work has suggested that anthropogenic processes may contribute to aerosol Fe in two ways. First, fossil-fuel combustion releases inorganic acids that can dissolve Fe from mineral dust (3, 4), and secondly it has been suggested that highly soluble Fe may be emitted directly during fossil-fuel combustion (3, 5, 6).

A variety of modeling and observational tools have been used to quantify the delivery of aerosol Fe to the oceans. Yet the leading models of Fe biogeochemistry prescribe aerosol Fe fluxes that vary over an order of magnitude from 1.4 to 32 Gmol y^{-1} (7). Estimates of ocean iron deposition from a suite of atmospheric aerosol models provide an even greater range: up to 535 Gmol y^{-1} (8). Atmospheric models also differ greatly on whether anthropogenic aerosols are a significant source of Fe to the oceans, with estimates of the fraction of soluble Fe delivered from anthropogenic aerosol emissions ranging from insignificant (9) to over half of the global supply of aerosol Fe (~66%) (10). Following deposition, anthropogenic Fe can dissolve in seawater and therefore can be available to support phytoplankton growth (3, 5, 8, 11–13). Uncertainties in the delivery of anthropogenic Fe are particularly pronounced for high-nutrient–low-chlorophyll (HNLC) regions, where other phytoplankton nutrients are abundant, but the flux of mineral Fe aerosols is low, resulting in Fe limitation of phytoplankton growth and reduced export of carbon to the deep ocean. This uncertainty stems from poor constraints on the magnitude of anthropogenic and mineral Fe sources, the size spectra of anthropogenic and mineral dust Fe and how size affects transport over the oceans, and the different solubilities of anthropogenic and mineral Fe (6, 14, 15).

Observational evidence also suggests an important, although difficult to quantify, supply of anthropogenic Fe to the global ocean. For example, it has been shown that higher concentrations of soluble Fe in aerosols are correlated with elevated concentrations of combustion products such as vanadium and black carbon (4, 16–18). This type of evidence confirms both the presence of anthropogenic Fe in the atmosphere and that anthropogenic Fe is highly soluble, increasing the importance of anthropogenic Fe as a source of Fe to phytoplankton living in the surface ocean.

Iron isotopes present a unique tool for tracking anthropogenic aerosol Fe. Iron from desert dust, including aerosols collected over the ocean, has a total bulk (HNO_3 and HF-digested) δ^{56}Fe and soluble (water- and seawater-soluble) δ^{56}Fe similar to continental values of +0.1‰ (6, 19, 20). Meanwhile, anthropogenically impacted aerosols collected in both the Atlantic and the Pacific Oceans have δ^{56}Fe as low as −1.6‰ and −1.72‰, respectively (6, 19, 21). Analysis of aerosols close to anthropogenic combustion sources have even lower δ^{56}Fe, which implies that the low isotopic signatures are a result of human activities such as combustion processes, rather than an effect of solubilization of mineral Fe from anthropogenic acids (21, 22). However, aerosol composition in the atmosphere is highly variable and informed by a relatively small number of observations, making it challenging to evaluate how much anthropogenic Fe is actually delivered to the ocean.

Significance

Mineral dust has long been considered an important source of Fe to the surface ocean, especially in remote areas away from continental margins. However, anthropogenic Fe derived from fossil-fuel burning may also contribute Fe to surface waters. Here we show in situ evidence of anthropogenic Fe in seawater, based on the concentrations and isotopic composition of Fe measured during a springtime cruise which transected the North Pacific Ocean. Our results suggest that anthropogenic Fe could play a globally important role in marine productivity and carbon cycling.

Author contributions: P.P.-G., E.V.A., M.J.F., D.M.K., and S.G.J. designed research; P.P.-G., N.J.H., R.M.B., E.V.A., M.J.F., B.B.C., A.E.W., S.F., D.M.K., and S.G.J. performed research; P.P.-G., N.J.H., R.M.B., E.V.A., M.J.F., B.B.C., A.E.W., S.F., D.M.K., and S.G.J. analyzed data; and P.P.-G. and S.G.J. wrote the paper with assistance from all authors.

The authors declare no competing interest.

This article is a PNAS Direct Submission.

Published under the PNAS license.

[1]To whom correspondence may be addressed. Email: papinedo@ldeo.columbia.edu.

This article contains supporting information online at https://www.pnas.org/lookup/suppl/doi:10.1073/pnas.2010315117/-/DCSupplemental.

First published October 22, 2020.

Downloaded by guest on June 29, 2021

Here we present results from a field campaign in May 2017 following a latitudinal transect along 158°W from 25° to 42°N in the central North Pacific Ocean (Fig. 1*A*), which is downwind from industrial emissions in east Asia. Iron isotope data, in conjunction with high-resolution analyses of other metals and nutrients, show in situ evidence of anthropogenic Fe in seawater. This finding suggests that anthropogenic fossil-fuel burning is delivering Fe to the North Pacific Ocean, potentially impacting phytoplankton growth and changing our understanding of the ways in which fossil-fuel combustion is affecting primary productivity in the global oceans.

Results and Discussion

Iron concentrations in the central North Pacific Ocean are low (~0.2 nM) toward the southern end of the transect in the North Pacific Subtropical Gyre and toward the northern end in the Subarctic North Pacific Ocean, but peak in the middle of the transect around 35°N (Fig. 1*B*). Similarly, the isotopic composition of dissolved Fe, δ^{56}Fe, was negative between 35° and 40°N ($-0.23‰ > \delta^{56}Fe > -0.65‰$), while higher δ^{56}Fe values were observed both to the north and the south ($0.13 > \delta^{56}Fe > -0.01$) (Fig. 2*A*). Based on the isotopic signatures of the various Fe sources to the ocean (*SI Appendix*, Fig. S1), this suggests that input of anthropogenic aerosol Fe accounts for the low δ^{56}Fe observed in surface waters. Continental margins are the only major marine source with such low δ^{56}Fe signatures, but there is no physical supply route of margin Fe to the surface ocean in this location (see discussion below). Other possible sources such as mineral aerosol Fe inputs are associated with positive δ^{56}Fe (6, 19, 20), and in situ processes (e.g., biological uptake of Fe) tend to increase δ^{56}Fe (23).

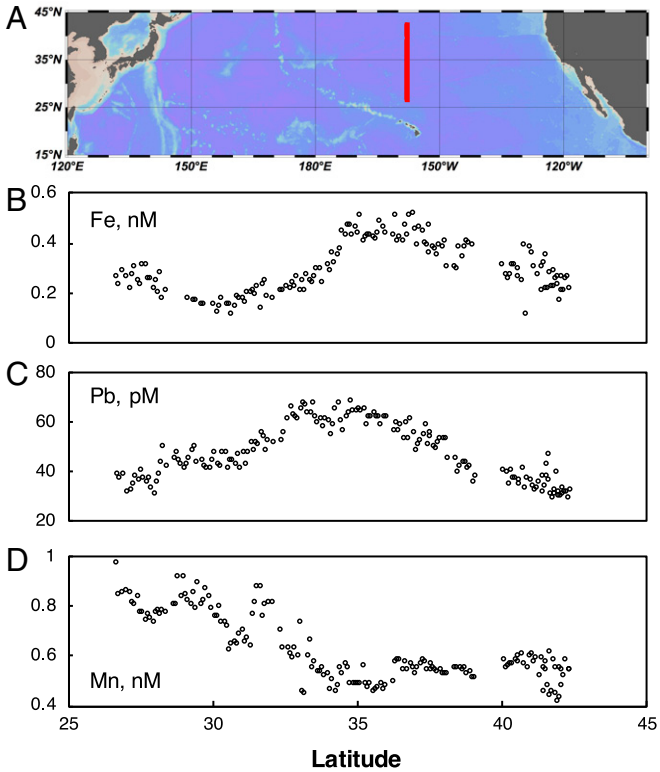

Fig. 1. High-resolution distribution of iron (Fe), lead (Pb), and manganese (Mn) across the North Pacific Ocean at 158°W from 21° to 42°N. (*A*) The red line indicates the cruise track. Samples were collected during the northbound leg. (*B*) Fe surface concentrations. (*C*) Pb surface concentrations. (*D*) Mn surface concentrations.

Satellite remote observations also support an atmospheric source of Fe. Desert dust storms and urban emissions lead to elevated aerosol concentrations over east Asia, traced by aerosol optical depth (AOD), which is blown out to sea by the westerly winds (Fig. 3). During April 2017, a band of high AOD overlapped with peak wind strength between 30° and 40°N, consistent with the high Fe concentrations measured during our transect.

An additional line of evidence supporting the deposition of aerosols from east Asia is the observed distribution of Pb and Pb isotopes. Surface Pb concentrations are also highest in the middle of the transect around 35°N, indicating a common source of both Pb and Fe (Fig. 1*C*). Nearly all of the Pb in the upper ocean today derives from anthropogenic Pb emissions to the atmosphere from high-temperature industrial activities such as coal burning, cement production, and the smelting of Pb and other metals. At lower temperatures Pb readily attaches to particles in both the atmosphere and ocean, giving it a residence time of a few weeks in the atmosphere and around 2 y in the surface ocean (24). Because different sources of Pb each have unique isotope signatures, Pb isotope ratios can be used to determine the recent source history of anthropogenic emissions. The isotopic composition of dissolved Pb was measured from the same nine surface samples collected for Fe isotopes. In our North Pacific Ocean sample set, we find $^{208}Pb/^{207}Pb$ and $^{206}Pb/^{207}Pb$ ratios similar to those in modern Asian aerosols, which are primarily attributable to Chinese industrial Pb emissions (25) (Fig. 2*B*). These Pb isotope signatures are distinct from Asian loess, deep Pacific Ocean dissolved Pb, and North American aerosols, suggestive of a recent deposition of anthropogenic aerosols rather than a dissolved source such as upwelling or advection from the Kuroshio current. There are slight differences in the distribution of Fe and Pb, notably the maximum in Pb occurring further to the south of the Fe maximum. This can be attributed to biological uptake of Fe between 32°–35°N earlier in the spring before macronutrients were depleted, as suggested by the higher satellite chlorophyll values registered at 32°N in February (0.21 mg m^{-3}) compared to those observed in May (0.07 mg m^{-3}) and the higher NO_3 concentrations measured in April 2016 (1 μM) than those observed in May 2017 (0.08 μM) (*SI Appendix*, Figs. S2 and S4).

To rule out deep water sources of Fe and Pb to the surface ocean, we examined the vertical distributions of both elements in the water column along the transect. Their distributions cannot support an upwelling supply of Fe and Pb, as both have surface maxima in the upper 30 m underlain by waters with lower concentrations (Fig. 4). Lateral sources of Fe from continental margin sediments to the subarctic North Pacific Ocean may supplement atmospheric sources, but they cannot explain surface enrichments found in the central North Pacific Ocean. Iron inputs from the North American margin occur at isopycnal layers with densities of sigma-theta ~26.5 (26, 27) while Fe inputs from the Asian margin carried into the North Pacific Ocean in the Kuroshio current occur at sigma-theta ~27 (28), corresponding to depths of 150 and 350 m at 35°N on our transect (Fig. 4). The vertical distribution of Mn also excludes a sedimentary source of Fe to the surface ocean at 35°N. Both Mn and Fe are released from reductive sediments (29, 30), so the marked differences between the vertical (Fig. 4) and surface (Fig. 1) distributions of Fe and Mn indicate independent sources, even accounting for their different redox behavior, biological removal, and cycling (29–31). Thus, based on these multiple lines of evidence we attribute the elevated Fe concentrations observed between 35°N and 40°N to recent aerosol deposition.

Iron isotope ratios can be used to constrain the amount of anthropogenic Fe supplied to the ocean, based on assumptions about the end-member δ^{56}Fe of anthropogenic Fe. We assume

Downloaded by guest on June 29, 2021

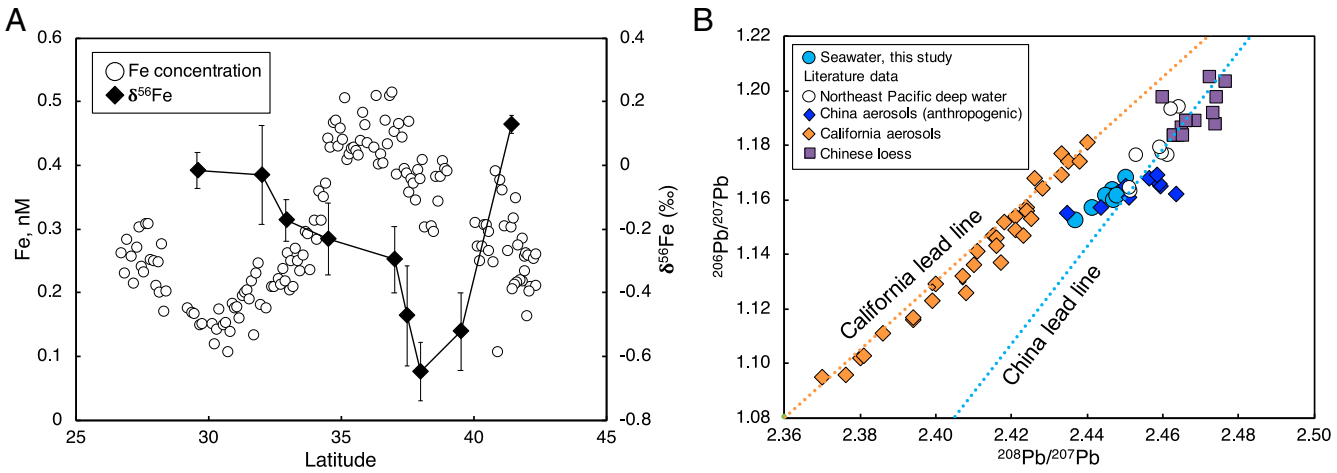

Fig. 2. (*A*) Distribution of surface Fe concentrations and stable isotope ratios (δ^{56}Fe) along the transect. (*B*) Pb isotope composition of seawater from the North Pacific Ocean compared to various Pb sources: North Pacific Ocean deep-water samples collected close to Hawaii below 500 m (52); Chinese aerosol samples collected since 2014 from sites with high levels of industrial emission (53–56); aerosols from California, which probably reflect a mixture between anthropogenic and natural Pb isotopes (57); Chinese loess samples (58). Data used to assess the isotopic composition of China and California lead lines are provided in *SI Appendix*, Table S1. Both Fe and Pb isotopes were measured from the same nine large-volume samples collected during the northbound leg.

that observations in the middle of the transect mostly reflect the δ^{56}Fe signature of recent aerosol deposition, with an average δ^{56}Fe of −0.54‰ for the three samples with the lowest δ^{56}Fe. These low δ^{56}Fe values are found in a region with high Fe/Pb ratios (between 35° and 40°N) (*SI Appendix*, Fig. S3), where we infer low Fe uptake, presumably due to limitation of phytoplankton growth by low macronutrient concentrations compared to the northerly waters (*SI Appendix*, Fig. S3). The δ^{56}Fe of anthropogenically influenced aerosols span a wide range, including values from −3.91 to +0.30‰ in the soluble phase for anthropogenically influenced aerosols collected in Japan (21, 22), with lower δ^{56}Fe typically found in small-size fractions that are most easily transported long distances to the central North Pacific Ocean. Here we apply an end-member δ^{56}Fe range from −1.6 to −1.8‰ for soluble anthropogenic Fe, based on the δ^{56}Fe values for Asian anthropogenically influenced aerosols (−1.8‰) (21, 22) and European and North American aerosols collected over the North Atlantic Ocean (−1.6‰) (6). The other end-member may include both mineral Fe delivered with the recent aerosol deposition event, as well as background dissolved Fe which was present before the recent deposition and which could have had either a mineral, anthropogenic, or other origin. Here we assume that the mineral dust δ^{56}Fe signature lies between +0.1 and +0.7‰, reflecting the range between soluble Fe leached directly from mineral aerosols (6, 20), and the upper range of dissolved δ^{56}Fe observed in dust-impacted North Atlantic Ocean surface waters (32). We assume a background dissolved δ^{56}Fe of 0 to +0.1‰, reflecting the range observed for the northerly and southerly samples from our transect, as well as near-surface samples from the oligotrophic North Pacific Ocean at 30°N, 130°W (33). The fraction of anthropogenic Fe in the recent deposition event which is attributable to anthropogenic aerosol Fe, as opposed to mineral aerosol Fe, is therefore estimated as between 21 and 59%. Recent estimates of the contribution of soluble Fe delivered to the North Pacific Ocean from anthropogenic aerosol emissions range over ∼1 order of magnitude (from 2 to 70%) (9, 10), and thus our calculated fraction of anthropogenic Fe encompasses a narrower range that can be used to better inform model parameterization.

Deposition fluxes of anthropogenic Fe to the study area can also be calculated, subject to certain assumptions. If the recent deposition observed in our measurements between 35°N and 40°N reflects the entire annual flux, and that flux is delivered to a 20-m mixed layer, the observed 0.4-nM surface ocean Fe would indicate a total annual aerosol soluble Fe flux of 8 μmol m^{-2} y^{-1}, of which 1.7–4.7 μmol m^{-2} y^{-1} (21–59%) is anthropogenic. If the residence time of Fe in the surface ocean is close to the lower bound of the 6–12-mo estimate for the oligotrophic North Pacific Ocean based on Th isotopes (34), the actual Fe flux might be larger. Additionally, our estimate of the fraction of anthropogenic Fe deposited in the study region is based on the assumption that biological productivity was limited by low macronutrient concentrations (NO_3 < 0.05 μM), and thus δ^{56}Fe can be used to directly apportion source, without extensive modification of the isotopic signature from Fe biological cycling. However, it is possible that anthropogenic Fe may stimulate productivity along the transect either by fueling nitrogen fixation (35) or during the winter and spring seasons when NO_3 concentrations are higher (*SI Appendix*, Fig. S5). If this were the case, and the observed δ^{56}Fe values were increased by in situ processes such as biological

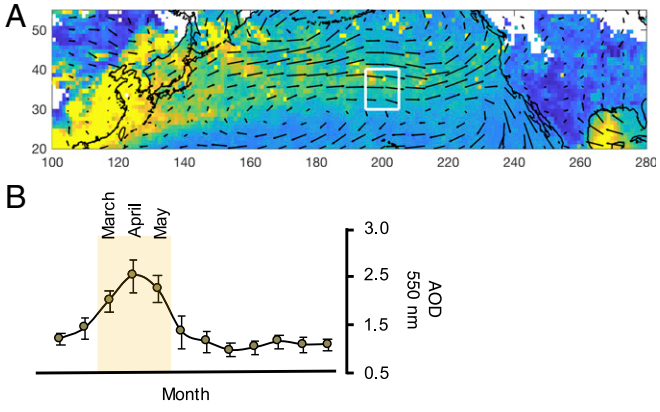

Fig. 3. Springtime satellite and climatological data across the North Pacific Ocean. (*A*) Aerosol optical depth from NASA's MODIS-A at 550 nm for April 2017 (color) with surface wind speed and direction (arrows) showing atmospheric circulation patterns. The white square represents the study area. (*B*) Monthly aerosol optical depth between 30° and 40°N averaged over the last 12 y.

Downloaded by guest on June 29, 2021

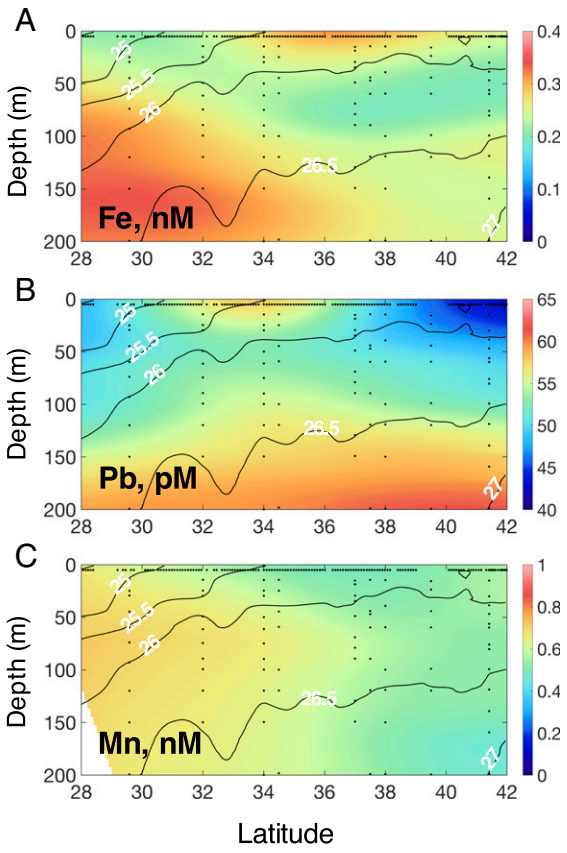

Fig. 4. Vertical distributions of elements in the upper water column along the transect. (*A*) Fe concentrations. (*B*) Pb concentrations. (*C*) Mn concentrations. Contour lines show density at 0.5-kg m^{-3} intervals. Samples were collected during the southbound leg.

uptake or adsorption onto particles (23, 36), the amount of anthropogenic Fe delivered from aerosols could be even higher.

The direct observation of anthropogenic Fe deposition in our study region implies that anthropogenic Fe is deposited throughout the North Pacific Ocean, although rapid biological cycling of Fe may preclude the use of δ^{56}Fe to trace this source in situ. Within the region where we observed the greatest input of anthropogenic Fe (35–40°N) along our transect, the input of anthropogenic aerosols is 140 μg m^{-2} y^{-1} based on the atmospheric models of Brahney et al. (37) and Chien et al. (38), gridded according to John et al. (39). Assuming similar concentrations of soluble Fe in all anthropogenic aerosols, we find that anthropogenic soluble Fe fluxes to the HNLC North Pacific Ocean range from 2 μmol m^{-2} y^{-1} in the eastern HNLC North Pacific to 68 μmol m^{-2} y^{-1} in the western HNLC North Pacific, with a mean flux of 10 μmol m^{-2} y^{-1} (Fig. 5). This flux is similar to estimates of pollution-induced deposition of soluble Fe based on atmospheric models including Goddard Earth Observing System (GEOS) (~3 μmol m^{-2} y^{-1} in the eastern HNLC North Pacific Ocean) (9, 40) and Community Atmosphere Model, version 4 (CAM4) (~4 μmol m^{-2} y^{-1}, in simulations with high anthropogenic Fe solubility) (6). A comparison of atmospheric model anthropogenic aerosol mass input to the study region (140 μg m^{-2} y^{-1}) with our inferred anthropogenic Fe flux to seawater (1.7–4.7 μmol m^{-2} y^{-1}, or 95–260 μg m^{-2} y^{-1}) suggests a high solubility of anthropogenic Fe (68–188%), and perhaps an underestimate of the total flux of anthropogenic aerosols.

Such large anthropogenic Fe fluxes could stimulate productivity in the HNLC North Pacific Ocean. Regions of predicted high deposition of anthropogenic Fe overlap with regions of high macronutrient concentrations in the HNLC North Pacific Ocean (37, 38) (Fig. 5). Anthropogenic soluble Fe deposition fluxes to HNLC waters (defined here as waters with at least 5 μM mean annual nitrate based on World Ocean Atlas data) correspond to surface ocean seawater Fe fluxes of 0.1–10 nM y^{-1}, assuming a 20-m mixed-layer depth throughout the North Pacific Ocean, potentially impacting productivity in the surface ocean and having large-scale impact on nutrient cycling. Effects may also be felt further afield. In fact, ocean biogeochemical modeling shows that the delivery of similar amounts of anthropogenic Fe to the North Pacific Ocean (1–6 μmol m^{-2} y^{-1}) would contribute to the expansion of oxygen minimum zones by increasing phytoplankton productivity (40).

A role for anthropogenic Fe also bears upon an understanding of macronutrient cycling in the North Pacific Ocean. Industrial emissions have been shown to be a significant source of fixed N to the North Pacific Ocean (40–43), potentially fueling productivity in the oligotrophic gyre and the Northwest Pacific Ocean. The increase in N availability caused by the deposition of pollutant N in conjunction with the deposition of aerosol Fe from anthropogenic sources could stimulate phytoplankton growth in the subtropics, and potentially switch parts of the subtropical Pacific Ocean from being N-limited to P-limited. Similar patterns in macronutrient concentrations have already been observed in high-latitude waters. Historical datasets appear to show variable declines in surface macronutrient concentrations throughout the HNLC North Pacific Ocean over the past few decades (44, 45), with a recent analysis suggesting that P and Si are declining at a rate of −0.012 ± 0.005 μmol l^{-1} $decade^{-1}$ and −0.38 ± 0.13 μmol l^{-1} $decade^{-1}$, while N concentrations are not declining (45). Changing macronutrient concentrations have typically been ascribed to physical processes, specifically warming of the surface ocean decreasing the mixed-layer depth, so that similar levels of phytoplankton productivity lead to greater nutrient depletion. Our finding that anthropogenic Fe may be delivered to surface waters of the HNLC North Pacific Ocean suggests that relief of Fe limitation may also contribute to patterns of nutrient drawdown and carbon export.

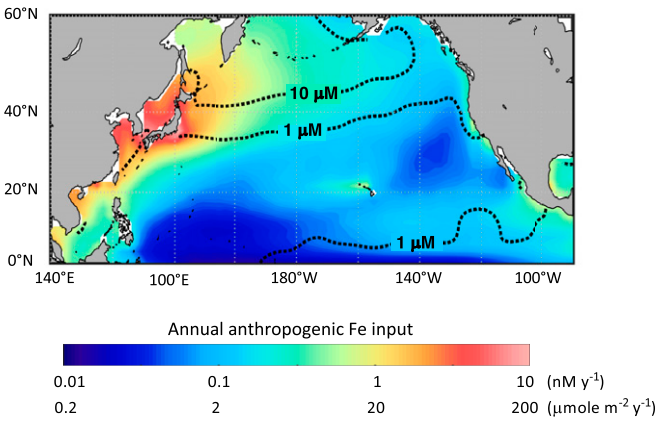

Fig. 5. Annual anthropogenic Fe input in the North Pacific Ocean. The likely region of anthropogenic Fe input overlaps with HNLC regions in the North Pacific Ocean. Annual anthropogenic Fe inputs are calculated at our study site, and then extrapolated across the North Pacific Ocean both as a surface flux (μmole m^{-2} y^{-1}) and a concentration flux assuming a 20-m mixed layer and 1-y residence time (nM y^{-1}) using anthropogenic mass deposition fluxes from Brahney et al. (37) and Chien et al. (38). Contours are World Ocean Atlas annual mean NO_3 (59), highlighting HNLC waters in the subarctic North Pacific Ocean.

Downloaded by guest on June 29, 2021

Materials and Methods

Sample Collection. Seawater samples were collected during the Simons Collaboration on Ocean Processes and Ecology (SCOPE)-Gradients expedition aboard the R/V Marcus G. Langseth in May 2017 (Figs. 1 and 4 and *SI Appendix*, Tables S2 and S3) during a latitudinal transect at 158°W from 25°N to 42°N. Surface seawater samples for the determination of trace metals and macronutrients were collected by two different methods during the northbound leg of the cruise. Subsurface samples were collected during the southbound leg in 8L external-spring Niskin bottles modified for trace-metal sampling with titanium and Delrin brackets (Ocean Test Equipment) mounted on an epoxy-coated rosette and deployed on a polypropylene (Amsteel) line. After collection, seawater was filtered through 0.2-μm Suporfilter cartridges into acid-washed 50-mL polypropylene centrifuge tubes (VWR Metal-Free).

High-resolution surface samples were collected every 30 min from a depth of roughly 10–15 m while underway at speeds of 9–12 kn. The inlet tube was kept at depth using a trace-metal clean surface tow fish system modified from Bruland et al. (46). The water intake tube was attached to a polyvinyl chloride (PVC) "vane" on a polypropylene line, with two PVC encapsulated lead weighted "torpedoes" and roughly 50 kg of steel weights mounted below the vane. The intake tubing was connected to a deck-mounted, compressed air-powered, polytetrafluoroethylene (PTFE) bellows pump (AstiPure II) to pump water at a rate of 5–10 L min^{-1}.

Subsamples were collected from the main water flow with an automated custom-made robotic fraction collector. This robot was controlled using an Arduino microcontroller to direct a moving sample collection arm and two peristaltic pumps. Sample drippers were attached to the collection arm which traveled over 50-mL centrifuge tubes (VWR Metal-free) mounted in a custom-made PVC base. The arm was moved by two Servo-powered linear actuators, a channel slider attached directly to the base, and a gear rack kit installed above the slider (ServoCity). Samples were pulled from the main water flow line through a T-junction by peristaltic pumps with a PTFE pump head (Cole Parmer MasterFlex) and filtered through 0.2-μm syringe filters (Pall Acrodisc Syringe Filter Supor membrane). For each sample, the Arduino was programmed to first turn on peristaltic pumps and dispense 20 mL to waste to clear the lines, then the sample arm moved the drippers over 50-mL centrifuge tubes and turned on for 90 s to collect 30–45 mL of sample. After sampling, the peristaltic pump was turned off and the arm returned to the waste position.

Analysis of Samples for Trace Metals. Seawater samples were analyzed for dissolved trace-metal concentrations at the University of Southern California after preconcentration using an offline adaptation of the *seaFAST*-pico metal extraction system (Elemental Scientific Inc.) as described in Lagerström et al. (47). Reagents were prepared with trace-metal clean water (Milli-Q), clean ammonium hydroxide (Optima), and acids prepared in a subboiling perfluoroalkoxy (PFA) still (Savillex). Briefly, using the *seaFAST*, 10-ml aliquots of seawater were extracted onto Nobias PA1 chelating resin at pH ~ 6.5 with an ammonium acetate/acetic acid buffer, then eluted in 10% vol/vol nitric acid (HNO_3). Fe, Ni, and Pb concentrations were measured by isotope dilution on a Thermo Fisher Element 2 high-resolution inductively coupled plasma mass spectrometry (HR-ICP-MS). The accuracy of our analytical procedure was verified by analysis of a seawater reference material (GS), for which good agreement with the reported consensus values were obtained, as shown in *SI Appendix*, Table S4.

Analysis of Samples for Nutrients. Discrete samples collected from the underway flow-through system ($n = 15$) as well as the conductivity, temperature, and depth (CTD)-rosette ($n = 98$) were analyzed for nitrate plus nitrite (N+N) and soluble reactive phosphorus (SRP, predominantly as phosphate) at the School of Ocean and Earth Science and Technology Laboratory for Analytical Biochemistry. Briefly, samples were run using an AA3 HR nutrient autoanalyzer, where N+N concentrations were determined using the colorimetric reaction of Strickland and Parsons (48), and SRP concentrations were determined following Murphy and Riley (49). The average precision for N+N was 0.3% and 0.5% for the 0–4 μmol L^{-1} and 0–43 μmol L^{-1} ranges, respectively, whereas for SRP it was 0.2% in the 0–2 μmol L^{-1} range. Accuracy was determined using National Metrology Institute of Japan (NMIJ)-certified reference standard solutions at 0.06 ± 0.02 μmol L^{-1} and 15.95 ± 0.5 μmol L^{-1} for N+N, and at 0.07 ± 0.01 μmol L^{-1} and 1.08 ± 0.05 μmol L^{-1} for SRP. Mean values for the NMIJ reference material obtained during the course of the runs were 0.08 ± 0.01 μmol L^{-1} and 16.18 ± 0.02 μmol L^{-1}, respectively, for N+N; and 0.08 ± 0.01 μmol L^{-1} and 1.08 ± 0.06 μmol L^{-1}, respectively, for SRP.

SRP was also analyzed in near-continuous mode via flow-through colorimetric methods (49) on a Technicon Auto Analyzer II coupled to a customized switching valve (Vici) that cycled through a set of standards including 1) filtered seawater from Station ALOHA with no added phosphate, and this same seawater with either 2) a final concentration of 300 nmol L^{-1} or 3) 700 nmol L^{-1} added P. Following these standards, the valve moved to an ~6-h analysis of surface seawater from the ship's flow-through system, after which another set of standards was run. This cycle (standards followed by a longer seawater run) was followed over the course of the cruise; however, we only present the outbound data here as standards were more stable over this period. The coefficient of variance of standards over the course of the outbound cruise track was between 10–16%. Raw voltages were first converted to SRP using the response factor of the running standards and reassessed postcruise via comparison to discrete SRP measurements described above. The slope of a type I linear regression of continuous SRP measurements and discrete measurements analyzed in shore-based laboratory was 1.06 ± 0.08 with an intercept of 15 ± 17 nmol L^{-1} and a R^2 value of 0.94 ($n = 15$).

Fe Isotope Analyses. Iron was extracted and purified for analysis from nine surface samples taken along the northbound surface transect in accordance with previously published methods (50). In this method, Fe is extracted from seawater using a bulk-extraction technique with Nobias PA-1 chelating resin after the addition of a ^{57}Fe - ^{58}Fe double spike. Following extraction, samples were purified by anion-exchange chromatography with AGMP-1 resin.

Iron isotope ratios were analyzed on a Thermo Neptune multicollector inductively coupled plasma mass spectrometry (MC-ICPMS) at the Center for Elemental Mass Spectrometry at the University of South Carolina. An ESI Apex-Q introduction system, 115 μL/min C100 Savillex Teflon nebulizer, and a combination of Jet sample and X skimmer cones were used. Analyses were conducted in high resolution following Faraday cup configuration: L3 (^{53}Cr), L2 (^{54}Fe and ^{54}Cr), L1 (^{56}Fe), C (^{57}Fe), H1 (^{58}Fe and ^{58}Ni), H2 (^{60}Ni), and H3 (^{61}Ni).

All uncertainties are expressed based on 2σ standard internal error of samples and standards as described in Conway et al. (50). Iron-stable isotope ratios are all reported in per mil (‰) relative to isotope standard IRRM-014 as follows.

Pb Isotope Analyses. Lead was extracted and purified for analysis from the same nine large-volume samples collected for Fe isotopes using a combination of previously published techniques. Pb was quantitatively extracted onto Nobias PA-1 resin using a batch extraction originally developed for Fe, Zn, and Cd isotope analysis (50), and was collected with other salts during column chromatographic purification of Fe, Zn, and Cd on AG-MP1 resin. Pb was further purified following the anion-exchange technique described in Reuer et al. (51).

Lead isotope ratios were analyzed on a Thermo Finnigan Neptune Plus MC-ICP-MS at the California Institute of Technology. An Apex desolvating system, 50 μL/min quartz nebulizer, and a combination of a Jet sample and X skimmer cones were used. Analyses were conducted in the static mode with the following Faraday cup configuration: L3 (^{202}Hg), L2 (^{203}Tl), L1 (^{204}Pb and ^{204}Hg), C (^{205}Tl), H1 (^{206}Pb), H2 (^{207}Pb), and H3 (^{208}Pb). A Tl single-element solution was added to both the standard and samples before the measurements at a Pb:Tl ratio of 4:1.

Data processing was conducted offline. The mass bias correction factor (f_{Tl}) was calculated following the exponential law (51) and using our measured $^{203}Tl/^{205}Tl$ ratios and the reference $^{203}Tl/^{205}Tl$ value of 0.41867. ^{204}Pb was corrected for isobaric interferences from ^{204}Hg by monitoring of ^{202}Hg and applying the f_{Tl} to the natural abundances of mercury isotopes (^{202}Hg = 0.2986 and ^{204}Hg = 0.0687). Finally, Pb isotope ratios were calculated using the exponential law and assuming $f_{Pb} = f_{Tl}$.

Analyses were calibrated with concurrent measurements of National Institute of Standards and Technology Standard Reference Materials (NIST SRM) 981 National Common Lead Isotopic Standard. Mean values ($n = 7 \pm 2$ SE) of NIST SRM 981 were $^{206}Pb/^{204}Pb$ = 16.933 ± 0.005, $^{207}Pb/^{204}Pb$ = 15.496 ± 0.004, $^{208}Pb/^{204}Pb$ = 36.715 ± 0.012, which show good agreement with reported certified values.

Fraction of Anthropogenic Fe Calculation. The fraction of dissolved Fe attributable to anthropogenic aerosols in the recent deposition event was calculated with a two-component mixing model:

Downloaded by guest on June 29, 2021

$$\delta^{56}Fe_{dissolved} = f_{mineral} \times \delta^{56}Fe_{mineral} + f_{anthropogenic} \times \delta^{56}Fe_{anthropogenic},$$

where is $f_{mineral}$ is the fraction of dissolved Fe from mineral aerosols and $f_{anthropogenic}$ is the fraction from anthropogenic aerosols. With $\delta^{56}Fe_{dissolved}$ from −0.30 to −0.65‰, $\delta^{56}Fe_{anthropogenic}$ from −1.6 to −1.8‰, and $\delta^{56}Fe_{mineral}$ from 0.1 to +0.7‰, and propagating uncertainties, we calculate that the fraction of dissolved Fe which originated in anthropogenic aerosols was between 21–59%. Total Fe concentrations in this region were between 0.3 and 0.5 nM, corresponding to concentrations of anthropogenic Fe between 0.07 and 0.29 nM.

Satellite Data Synthesis. Dust supply to the North Pacific Ocean was evaluated using monthly averaged 1° maps of AOD as a proxy for atmospheric dust concentration. Monthly Gridded Atmospheric Products from Moderate-Resolution Imaging Aqua (MODIS AQUA) (MYD08_M3) between 2003–2018 were downloaded from The Level-1 Atmosphere Archive & Distribution System (LAADS) Distributed Active Archive Center (DAAC) (https://ladsweb.modaps.eosdis.nasa.gov/). AOD at 550 nm was mapped using the Dark Target/Deep Blue Combined algorithm (https://www.atmos-meas-tech.net/6/2989/2013/amt-6-2989-2013.html). Values were averaged between 30°–40°N and 155°–165°W with null values excluded. These means were then averaged by month to produce an annual climatology.

Global monthly wind field at 20 m (Fleet Numerical Meteorology and Oceanography Center [FNMOC], 1°) were accessed for April 2017 from National Oceanic and Atmospheric Administration (NOAA) Environmental Research Divisions Data Access Program (ERDDAP) (https://coastwatch.pfeg.noaa.gov/erddap/index.html). This product is altered from its native resolution to 3° × 3° means.

Data Availability. All study data are included in the article and *SI Appendix*.

ACKNOWLEDGMENTS. This research was supported by the Simons Foundation (Award 426570SP to E.V.A., M.J.F., A.E.W., D.M.K., and S.G.J.). We thank the captain and crew of R/V *Marcus G. Langseth* for help during the sampling campaign.

1. P. W. Boyd, M. J. Ellwood, The biogeochemical cycle of iron in the ocean. *Nat. Geosci.* **3**, 675–682 (2010).
2. T. D. Jickells *et al*., Global iron connections between desert dust, ocean biogeochemistry, and climate. *Science* **308**, 67–71 (2005).
3. R. A. Scanza *et al*., Atmospheric processing of iron in mineral and combustion aerosols: Development of an intermediate-complexity mechanism suitable for Earth system models. *Atmos. Chem. Phys.* **18**, 14175–14196 (2018).
4. P. Y. Chuang, R. M. Duvall, M. M. Shafer, J. J. Schauer, The origin of water soluble particulate iron in the Asian atmospheric outflow. *Geophys. Res. Lett.* **32**, L07813 (2005).
5. H. Matsui *et al*., Anthropogenic combustion iron as a complex climate forcer. *Nat. Commun.* **9**, 1593 (2018).
6. T. M. Conway *et al*., Tracing and constraining anthropogenic aerosol iron fluxes to the North Atlantic Ocean using iron isotopes. *Nat. Commun.* **10**, 2628 (2019).
7. A. Tagliabue *et al*., How well do global ocean biogeochemistry models simulate dissolved iron distributions? *Global Biogeochem. Cycles* **30**, 149–174 (2016).
8. S. Myriokefalitakis *et al*., Reviews and syntheses: The GESAMP atmospheric iron deposition model intercomparison study. *Biogeosciences* **15**, 6659–6684 (2018).
9. M. S. Johnson, N. Meskhidze, Atmospheric dissolved iron deposition to the global oceans: Effects of oxalate-promoted Fe dissolution, photochemical redox cycling, and dust mineralogy. *Geosci. Model Dev. Discuss* **6**, 1901–1947 (2013).
10. S. Myriokefalitakis *et al*., Changes in dissolved iron deposition to the oceans driven by human activity: A 3-D global modelling study. *Biogeosciences* **12**, 3973–3992 (2015).
11. A. Ito, Z. Shi, Delivery of anthropogenic bioavailable iron from mineral dust and combustion aerosols to the ocean. *Atmos. Chem. Phys.* **16**, 85–99 (2016).
12. C. Luo *et al*., Combustion iron distribution and deposition. *Global Biogeochem. Cycles* **22**, GB1012 (2008).
13. A. Ito *et al*., Pyrogenic iron: The missing link to high iron solubility in aerosols. *Sci. Adv.* **5**, u7671 (2019).
14. M. C. Todd *et al*., Quantifying uncertainty in estimates of mineral dust flux: An intercomparison of model performance over the Bodélé Depression, northern Chad. *J. Geophys. Res.* **113**, D24107 (2008).
15. N. M. Mahowald *et al*., Aerosol trace metal leaching and impacts on marine microorganisms. *Nat. Commun.* **9**, 2614 (2018).
16. P. N. Sedwick, E. R. Sholkovitz, T. M. Church, Impact of anthropogenic combustion emissions on the fractional solubility of aerosol iron: Evidence from the Sargasso Sea. *Geochem. Geophys. Geosyst.* **8**, Q10Q06 (2007).
17. E. R. Sholkovitz, P. N. Sedwick, T. M. Church, Influence of anthropogenic combustion emissions on the deposition of soluble aerosol iron to the ocean: Empirical estimates for island sites in the North Atlantic. *Geochim. Cosmochim. Acta* **73**, 3981–4003 (2009).
18. H. Chen *et al*., Coal fly ash as a source of iron in atmospheric dust. *Environ. Sci. Technol.* **46**, 2112–2120 (2012).
19. C. Mead, P. Herckes, B. J. Majestic, A. D. Anbar, Source apportionment of aerosol iron in the marine environment using iron isotope analysis. *Geophys. Res. Lett.* **40**, 5722–5727 (2013).
20. M. Waeles, A. R. Baker, T. Jickells, J. Hoogewerff, Global dust teleconnections: Aerosol iron solubility and stable isotope composition. *Environ. Chem.* **4**, 233–237 (2007).
21. M. Kurisu *et al*., Variation of iron isotope ratios in anthropogenic materials emitted through combustion processes. *Chem. Lett.* **45**, 970–972 (2016).
22. M. Kurisu, Y. Takahashi, T. Iizuka, M. Uematsu, Very low isotope ratio of iron in fine aerosols related to its contribution to the surface ocean. *J. Geophys. Res. Atmos.* **121**, 11119–11136 (2016).
23. M. J. Ellwood *et al*., Iron stable isotopes track pelagic iron cycling during a subtropical phytoplankton bloom. *Proc. Natl. Acad. Sci. U.S.A.* **112**, E15–E20 (2015).
24. Y. Echegoyen *et al*., Recent distribution of lead in the Indian Ocean reflects the impact of regional emissions. *Proc. Natl. Acad. Sci. U.S.A.* **111**, 15328–15331 (2014).
25. X.-Y. Bi *et al*., Lead isotopic compositions of selected coals, Pb/Zn ores and fuels in China and the application for source tracing. *Environ. Sci. Technol.* **51**, 13502–13508 (2017).
26. P. J. Lam *et al*., Wintertime phytoplankton bloom in the Subarctic Pacific supported by continental margin iron. *Global Biogeochem. Cycles* **20**, GB1006 (2006).
27. P. J. Lam, J. K. B. Bishop, The continental margin is a key source of iron to the HNLC North Pacific Ocean. *Geophys. Res. Lett.* **35**, L07608 (2008).
28. J. Nishioka, H. Obata, Dissolved iron distribution in the western and central subarctic Pacific: HNLC water formation and biogeochemical processes. *Limnol. Oceanogr.* **62**, 2004–2022 (2017).
29. W. M. Landing, K. W. Bruland, Manganese in the North Pacific. *Earth Planet. Sci. Lett.* **49**, 45–56 (1980).
30. Z.-W. Wang *et al*., Geochemical behavior of dissolved manganese in the East China Sea: Seasonal variation, estuarine removal, and regeneration under suboxic conditions. *Geochem. Geophys. Geosyst.* **17**, 282–299 (2016).
31. M. Hatta *et al*., An overview of dissolved Fe and Mn distributions during the 2010-2011 U.S. GEOTRACES North Atlantic cruises: GEOTRACES GA03. *Deep. Res. Part II Top. Stud. Oceanogr.* **116**, 117–129 (2015).
32. S. G. John, T. M. Conway, A role for scavenging in the marine biogeochemical cycling of zinc and zinc isotopes. *Earth Planet. Sci. Lett.* **394**, 159–167 (2014).
33. T. M. Conway, S. G. John, The cycling of iron, zinc and cadmium in the North East Pacific Ocean–Insights from stable isotopes. *Geochim. Cosmochim. Acta* **164**, 262–283 (2015).
34. C. T. Hayes *et al*., Thorium isotopes tracing the iron cycle at the Hawaii Ocean Time-series Station ALOHA. *Geochim. Cosmochim. Acta* **169**, 1–16 (2015).
35. C. M. Moore *et al*., Large-scale distribution of Atlantic nitrogen fixation controlled by iron availability. *Nat. Geosci.* **2**, 867–871 (2009).
36. M. J. Ellwood *et al*., Distinct iron cycling in a Southern Ocean eddy. *Nat. Commun.* **11**, 825 (2020).
37. J. Brahney, N. Mahowald, D. S. Ward, A. P. Ballantyne, J. C. Neff, Is atmospheric phosphorus pollution altering global alpine Lake stoichiometry? *Global Biogeochem. Cycles* **29**, 1369–1383 (2015).
38. C. Te Chien *et al*., Effects of African dust deposition on phytoplankton in the western tropical Atlantic Ocean off Barbados. *Global Biogeochem. Cycles* **30**, 716–734 (2016).
39. S. G. John *et al*., AWESOME OCIM: A simple, flexible, and powerful tool for modeling elemental cycling in the oceans. *Chem. Geol.* **533**, 119403 (2020).
40. T. Ito, A. Nenes, M. S. Johnson, N. Meskhidze, C. Deutsch, Acceleration of oxygen decline in the tropical Pacific over the past decades by aerosol pollutants. *Nat. Geosci.* **9**, 443–447 (2016).
41. T. W. Kim, K. Lee, R. G. Najjar, H.-D. Jeong, H. J. Jeong, Increasing N abundance in the northwestern Pacific Ocean due to atmospheric nitrogen deposition. *Science* **334**, 505–509 (2011).
42. C. Zhang *et al*., Fertilization of the northwest Pacific Ocean by east Asia air pollutants. *Global Biogeochem. Cycles* **33**, 690–702 (2019).
43. I. N. Kim *et al*., Chemical oceanography. Increasing anthropogenic nitrogen in the North Pacific Ocean. *Science* **346**, 1102–1106 (2014).
44. F. A. Whitney, H. J. Freeland, Variability in upper-ocean water properties in the NE Pacific Ocean. *Deep Sea Res. Part II Top. Stud. Oceanogr.* **46**, 2351–2370 (1999).
45. S. Yasunaka *et al*., Long-term variability of surface nutrient concentrations in the North Pacific. *Geophys. Res. Lett.* **43**, 3389–3397 (2016).
46. K. W. Bruland, E. L. Rue, G. J. Smith, G. R. DiTullio, Iron, macronutrients and diatom blooms in the Peru upwelling regime: Brown and blue waters of Peru. *Mar. Chem.* **93**, 81–103 (2005).
47. M. E. Lagerström *et al*., Automated on-line flow-injection ICP-MS determination of trace metals (Mn, Fe, Co, Ni, Cu and Zn) in open ocean seawater: Application to the GEOTRACES program. *Mar. Chem.* **155**, 71–80 (2013).

Downloaded by guest on June 29, 2021

48. J. D. Strickland, T. R. Parsons, *A Practical Handbook of Seawater Analysis*, (Fisheries Research Board of Canada, Ottawa, Canada, 1972), pp. 65–70.
49. J. Murphy, J. P. Riley, A modified single solution method for the determination of phosphate in natural waters. *Anal. Chim. Acta* **27**, 31–36 (1962).
50. T. M. Conway, A. D. Rosenberg, J. F. Adkins, S. G. John, A new method for precise determination of iron, zinc and cadmium stable isotope ratios in seawater by double-spike mass spectrometry. *Anal. Chim. Acta* **793**, 44–52 (2013).
51. M. K. Reuer, E. A. Boyle, B. C. Grant, Lead isotope analysis of marine carbonates and seawater by multiple collector ICP-MS. *Chem. Geol.* **200**, 137–153 (2003).
52. C. M. Zurbrick, C. Gallon, A. R. Flegal, Historic and industrial lead within the Northwest Pacific Ocean evidenced by lead isotopes in seawater. *Environ. Sci. Technol.* **51**, 1203–1212 (2017).
53. X. Hu *et al*., Lead contamination and transfer in urban environmental compartments analyzed by lead levels and isotopic compositions. *Environ. Pollut.* **187**, 42–48 (2014).
54. N. Gai *et al*., Selected organochlorine pesticides and polychlorinated biphenyls in atmosphere at Ruoergai high altitude prairie in eastern edge of Qinghai-Tibet Plateau and their source identifications. *Atmos. Environ.* **95**, 89–95 (2014).
55. N. Dewan *et al*., Effect of pollution controls on atmospheric PM2.5 composition during Universiade in Shenzhen, China. *Atmosphere* **7**, 57 (2016).
56. Z. Q. Zhao *et al*., Atmospheric lead in urban Guiyang, Southwest China: Isotopic source signatures. *Atmos. Environ.* **115**, 163–169 (2015).
57. A. M. Pierce, M. S. Gustin, J. N. Christensen, S. M. Loría-Salazar, Use of multiple tools including lead isotopes to decipher sources of ozone and reactive mercury to urban and rural locations in Nevada, USA. *Sci. Total Environ.* **615**, 1411–1427 (2018).
58. F. Wu, S. S. H. Ho, Q. Sun, S. H. S. Ip, Provenance of Chinese loess: Evidence from stable lead isotope. *Diqiu Kexue Jikan* **22**, 305–314 (2011).
59. H. E. Garcia *et al*., *World Ocean Atlas 2009, Volume 4: Nutrients (Phosphate, Nitrate, and Silicate)*, (U.S. Department of Commerce National Oceanic and Atmospheric Administration, 2010).

Downloaded by guest on June 29, 2021